Electronic Supplementary Material (ESI) for Soft Matter.

Electronic Supplementary Information

Mechanical phase inversion of Pickering emulsions via metastable wetting of rough colloids

Michele Zanini,[†§‡] Alberto Cingolani,[⊥‡] Chiao-Peng Hsu,[†] Miguel Angel Fernandez Rodriguez,[†] Giuseppe Soligno,[&] Anna Beltzung,[⊥] Stefano Caimi,[⊥] Denise Mitrano,[#] Giuseppe Storti[⊥] and Lucio Isa[†]*

† Laboratory for Soft Materials and Interfaces, Department of Materials, ETH Zürich, Zürich (Switzerland)

§ Van 't Hoff Laboratory for Physical and Colloid Chemistry, Debye Institute for Nanomaterials Science, Utrecht University, Utrecht (The Netherlands)

& Condensed Matter and Interfaces, Debye Institute for Nanomaterials Science, Utrecht University, Utrecht (The Netherlands)

⊥ Department of Chemistry and Applied Biosciences, Institute for chemical and bioengineering, ETH Zürich, Zürich (Switzerland)

Process Engineering Department, Eawag, Swiss Federal Institute of Aquatic Science and Technology (Switzerland)

*** Corresponding Author: lucio.isa@mat.ethz.ch**

Table of content

Supplementary Tables

Table S1 Recipes for emulsion polymerization of the smooth reference particles.

		Core		**Shell**
		Weight %		
		IC_S	**$CF1_S$**	**$CF2_S$**
PS-I	H_2O	99.8	49	-
	SDS	0.2	1	-
	St	-	40	98.5
	DVB	-	10	1.5

Table S2 Recipes for emulsion polymerization of the rough core-shell particles with different morphologies.

		Core	**Shell**	
		Weight %		
		IC_R	**$CF1_R$**	**$CF2_R$**
PS-II	H2O	90	66	-
	SDS	0.3	0.6	-
	AN	10	-	-
	St	-	32.4	-
	DVB	-	1	-
	KPS	0.3	-	-
		IC_R	**$CF1_R$**	**$CF2_R$ (60 min)**
PS-III	H2O	90	66	65.7
	SDS	0.3	0.3	1.3
	AN	10	33.7	-
	St	-	-	32
	DVB	-	-	1
	KPS	0.3	-	-
		IC_R	**$CF1_R$**	**$CF2_R$ (210 min)**
PS-IV	H2O	90	66	65.7
	SDS	0.3	0.3	1.3
	AN	10	33.7	-
	St	-	-	31.4
	DVB	-	-	1.6
	KPS	0.3	-	-

Table S3 Size and polydispersity of the obtained organic particles measured by SEM and AFM.

	PS-I	**PS-II**	**PS-III**	**PS-IV**
Diameter SEM (nm)	68±4	120±10	164±8	158±10
Diameter AFM (nm)	64±12	114±16	172±30	170±26

Table S4 Reaction parameters for the fabrication of inorganic raspberry-like particles. The reported quantities were used to modify 50 mg of particles.

Name	**Core diameter (nm)**	**NP diameter (nm)**	**Injected TEOS (5 vol%)(mL)**	δ
SiO_2-II	161 ± 15	22	0.65	1.05 ± 0.23
SiO_2-III	588 ± 21	22	1.3	1.52 ± 0.26
SiO_2-IV	374 ± 14	39	1.3	3.46 ± 0.94

Table S5 Estimation of the energy barrier for contact line relaxation. $\gamma_{decane\text{-}water}$ = 53 mNm^{-1}, $\gamma_{cineole\text{-}water}$ = 16.9 mNm^{-1}. The asperity height and mean asperity distance are estimated from AFM images. Green cells indicate the possibility that particles can be transferred through the interface while red ones the impossibility. The combinations reported in yellow have not been tested since redundant.

	Mean asperity Height (nm)	Mean asperity Distance (nm)	Number of asperities at equator	Depinning single asperity from water/n-decane (10^3 k_BT)	Depinning from equator Water/n-decane (10^3 k_BT)	Phase inversion	Depinning single asperity from water/cineole (10^3 k_BT)	Depinning from equator Water/cineole (10^3 k_BT)	Phase inversion
PS-II	13.6 ± 3.4	62 ± 30	6.1 ± 3	2 ± 0.6	12.0±6.9		0.6 ± 0.2	3.8±2.2	
SiO_2-II	24.8 ± 4.1	68 ± 4	18 ± 2.1	6 ± 1.2	107.3±24.2		1.9 ± 0.4	34.2±7.7	
SiO_2-III	23.8 ± 3.6	71 ± 5	28.5 ± 2.1	5.5 ± 1	156.3±30.9		1.7 ± 0.3	49.8±9.9	
SiO_2-IV	39 ± 7.2	52 ± 10	29 ± 5.7	14.7 ± 3.1	427.1±122.9		4.7 ± 1	136.2±39.2	

Supplementary Figures

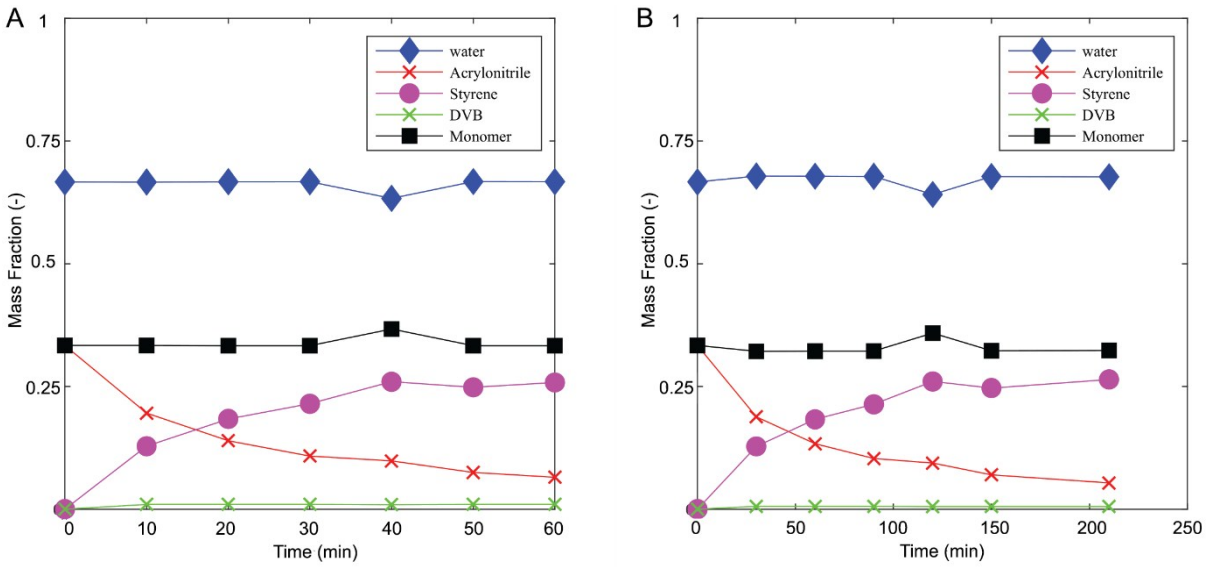

Figure S1 Evolution of the feed composition (mass fractions) for PS-III (A) and PS-IV (B).

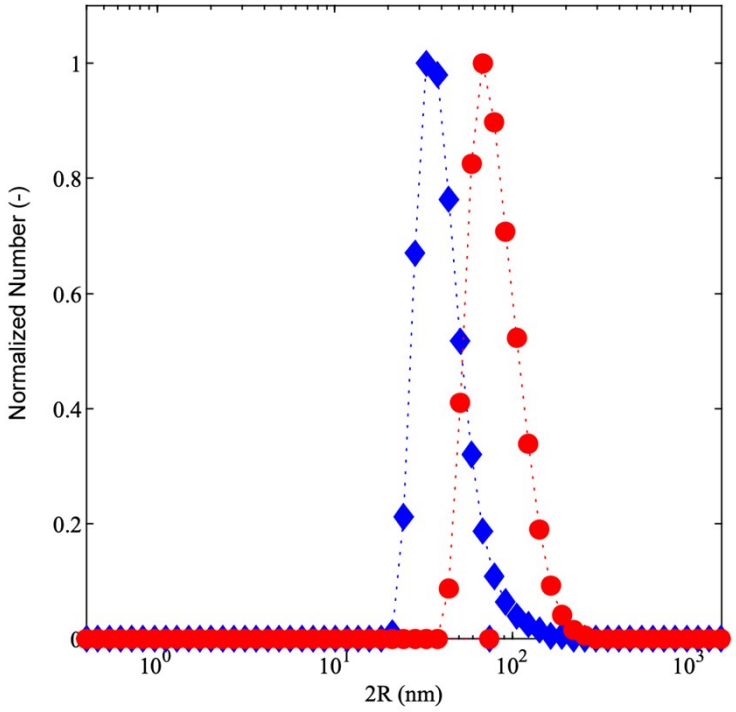

Figure S2 DLS data for PS-I and PS-II dispersed in milliQ water.

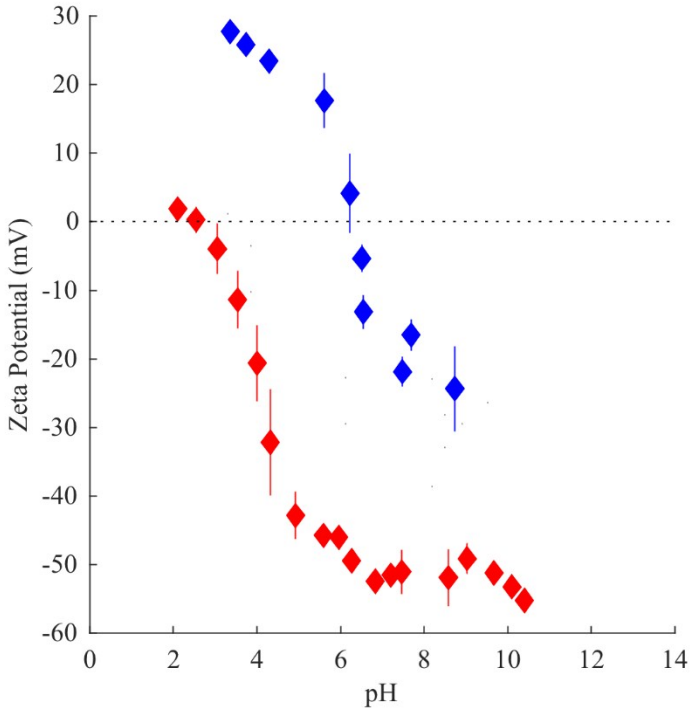

Figure S3 Titration curves of silica rough particles (SiO_2-III). Red symbols represent the results obtained for the pristine colloidal particles. Blue diamonds describe the trend for amino-functionalized SiO_2-III. The shift of the isoelectric point is used as a confirmation of the successful functionalization with amino-silanes.

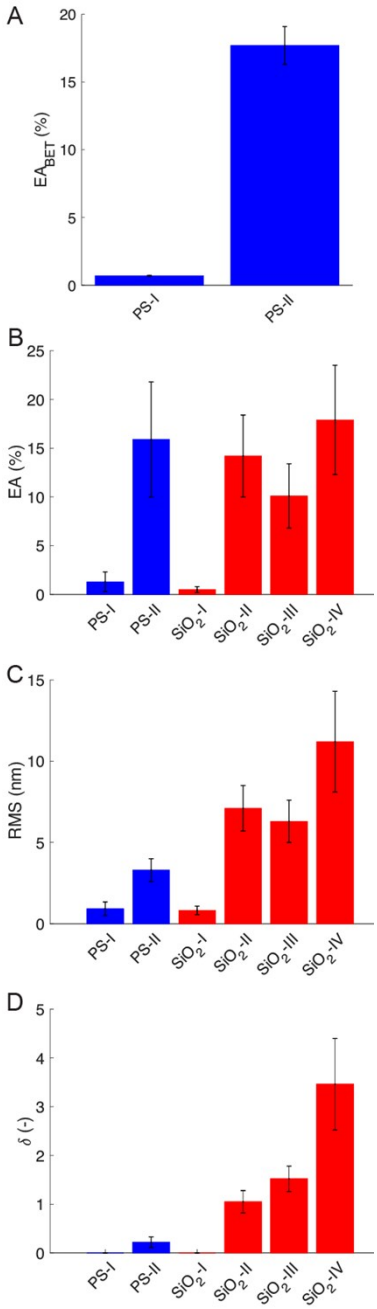

Figure S4 Comparison among different roughness descriptors. The surface roughness of the various colloids expressed in terms of (A) normalized excess area from BET (EA_{BET}), (B) excess area (EA), (C) root-mean square roughness (RMS) and (D) dimensionless roughness parameter δ (as in the main manuscript) for organic (blue) and inorganic (red) particles.

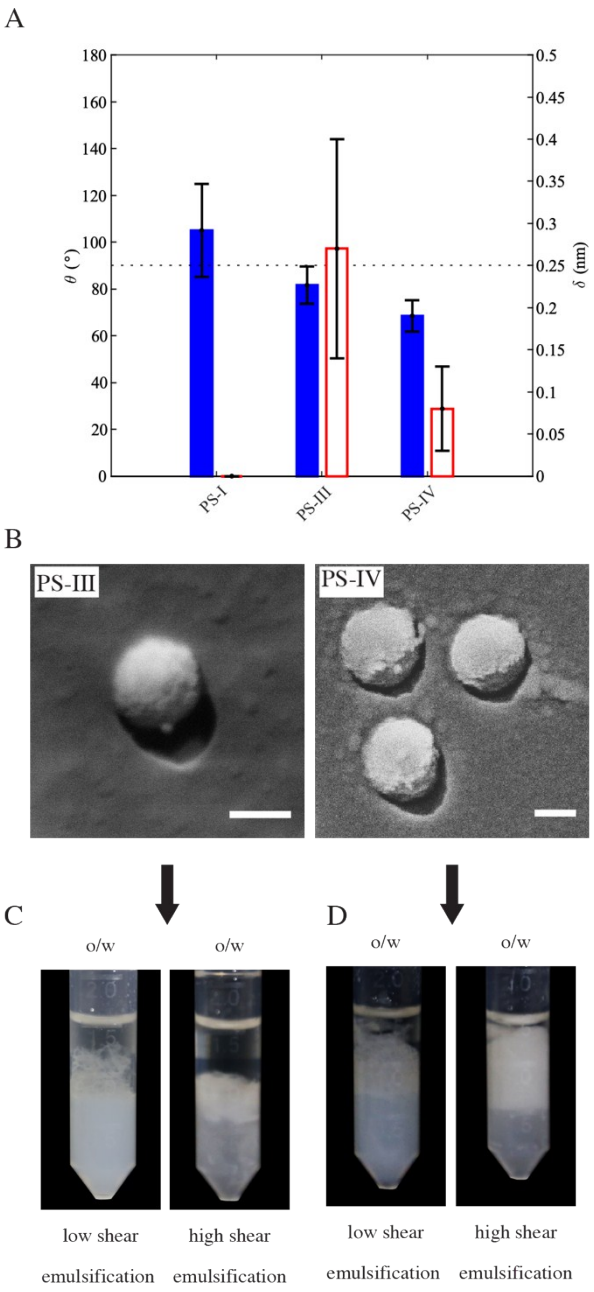

Figure S5 (A) Contact angle and δ for the synthetized organic colloids. Left axis corresponds to the water/n-decane contact angle θ plotted with the filled bars. The roughness parameter associated to the surface morphology is reported on the right axis and plotted with empty bars. (B) Wetting of organic colloids with similar surface morphology and bulk chemistry studied with FreSCa cryo-SEM. Scale bars 100 nm. (C) are macroscopic images of emulsions obtained using 1:1 water (0.1 wt%):n-decane using PS-III and PS-IV, at high and low shear rates, respectively.

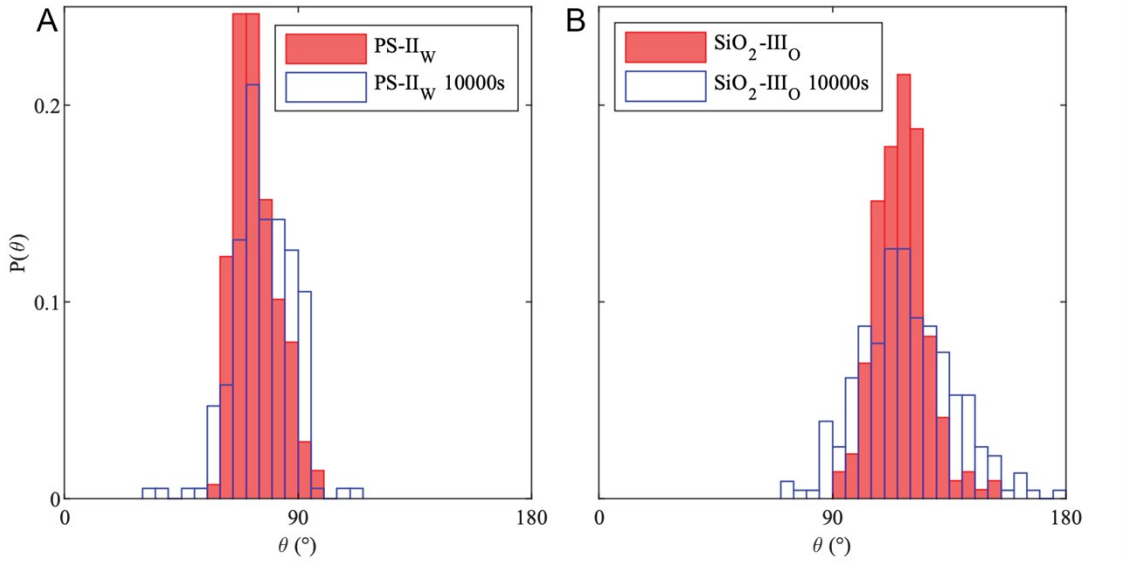

Figure S6 Ageing of the contact angle at flat water/n-decane for PS-II$_W$ and SiO_2-III$_O$ in (A) and (B), respectively. Filled and empty bars respectively represent the contact angle distributions when the adsorption is arrested upon shock-freezing after about 1 min and 10000 s after the generation of the interface.

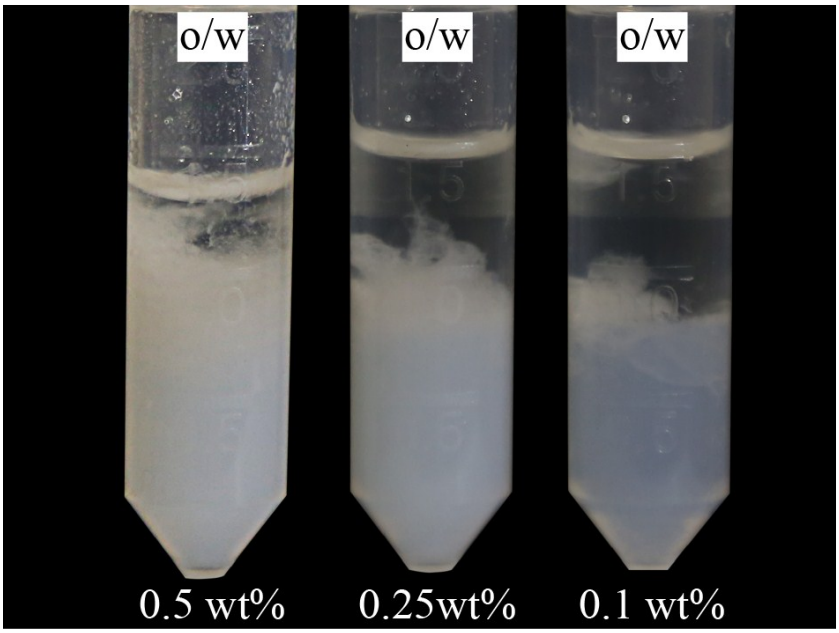

Figure S7 Emulsions of water and n-decane (1:1) stabilized by PS-II; created at low shear rates. As expected, higher solid loading of organic rough particles can stabilize larger volumes of dispersed phase.

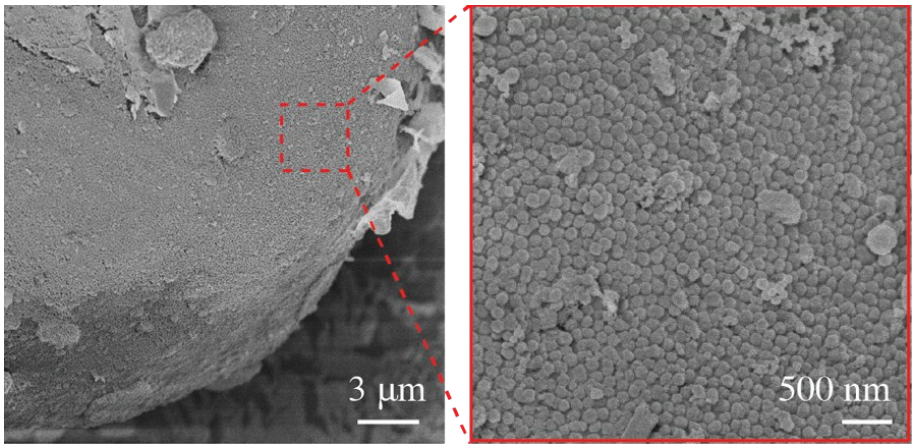

Figure S8 FreSCa cryo-SEM images of the PS-II particles on w/o emulsion droplets produced at high emulsification energy (12000 rpm with T25 ULTRA-TURRAX) for 3 minutes.

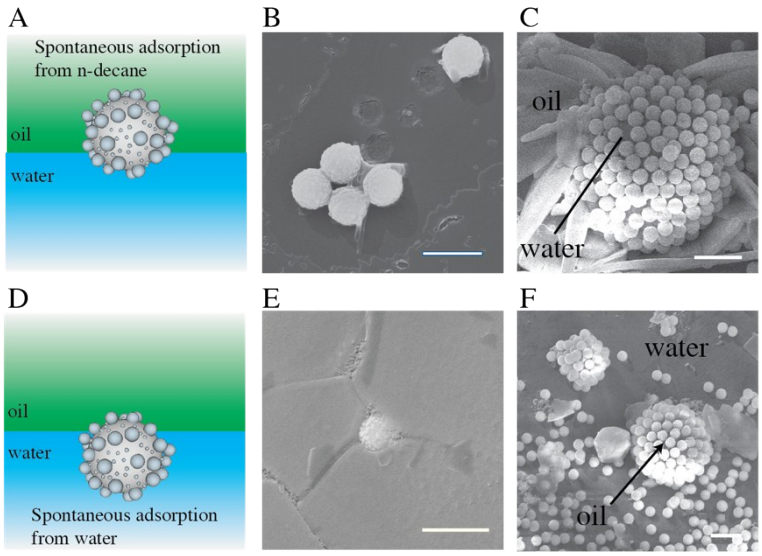

Figure S9 Spontaneous adsorption and Pickering stabilization. **(A-C)** SiO_2-III_O adsorbs from n-decane. **(D-F)** SiO_2-III_W adsorbs from water. The schematics of the rough colloids spontaneously adsorbing from two the different phases are represented in **(A)** and **(D)**. The corresponding FreSCa images are reported in **(B)** and **(E)**. Pickering emulsions stabilized with SiO_2-III emulsified at low shear rates. In **(C)** the colloids are initially dispersed in n-decane (Figure 6G main manuscript). In **(F)** the colloids are initially dispersed in water (Figure 6B main manuscript).

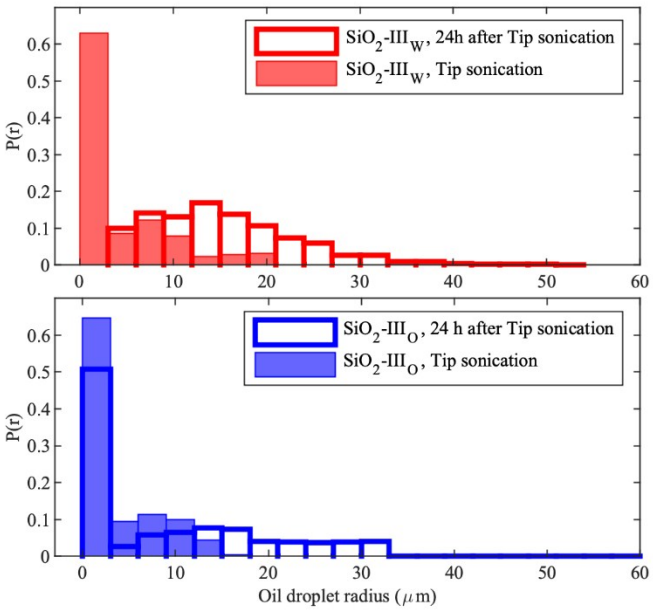

Figure S10 Droplet size evolution within 24 h for emulsions reported in Figure 6 E (SiO_2-IIIW) and J (SiO_2-IIIO) of the main manuscript.

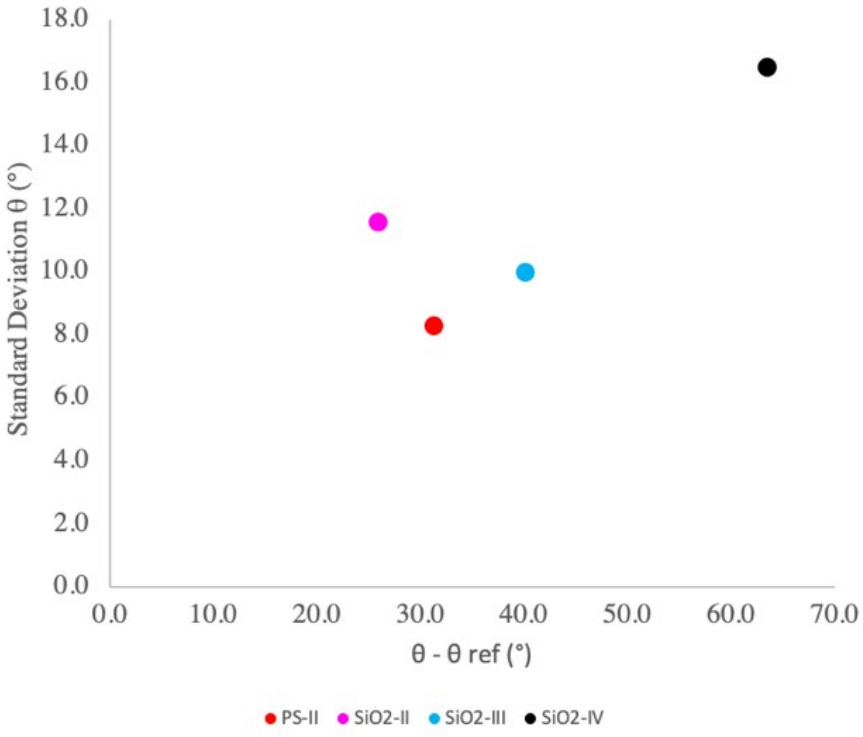

Figure S11 Relation between the width of the contact angle distribution and the difference between the mean measured contact angle for rough colloids (θ) and their smooth reference (θ_{ref}).

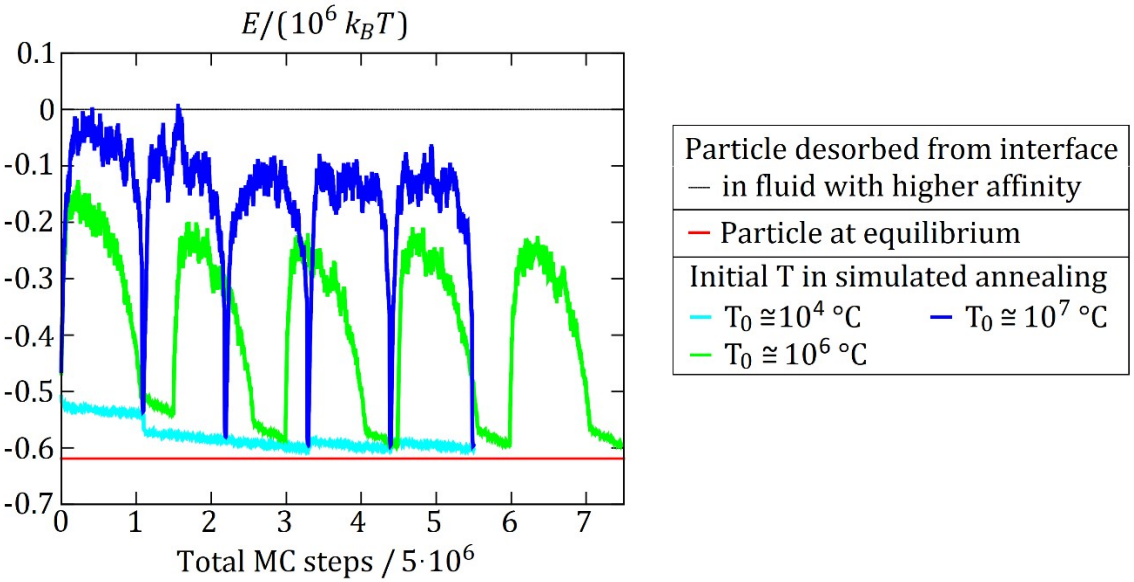

Figure S12 Energy E (corresponding to the interface shape) plotted every 5000 Monte Carlo steps during three quasi-static simulations (consisting of 5 simulated-annealing simulations each, with each simulated-annealing simulation consisting of ~10^7 Monte Carlo steps). For each quasi-static simulation, the initial temperature T_0 used in the simulated-annealing simulations is $(cyan)\ 10^4$ °C,$(green)\ 10^6$ °C, $(blue)10^7$ °C (then, the temperature is decreased linearly thorough the simulated annealing till zero). The colloid is initially at its equilibrium height at the interface, thus E for the initial interface shape in the first simulated-annealing simulation is close to the energy of a particle at equilibrium (slightly higher, since the simulation starts using as initial interface shape a flat plane, i.e. not including capillary deformations).

SI 1: Stability of PS-I and PS-II in milliQ water

Charge-stabilized, organic rough particles are stable in aqueous solutions despite their mild hydrophobic nature when trapped at a n-decane/water interface. This is confirmed by the monomodal size distribution measured in DLS measurements (**Figure S2**). The data are here reported in number distribution in analogy to the sizing of the particle that has been performed via SEM pictures image analysis. The sample is relatively polydisperse, and a fraction of dumbbells is present in the system.

SI 2: AFM roughness extraction and comparison among roughness operators

To extract the proper surface roughness, we decoupled the topographical signal of interest from the underlying particle curvature by means of a custom-written algorithm based on a least-squares approach. The latter finds the unique sphere that closely encompasses the scanned particle. Both the position of the particle center and its radius are determined as adjustable parameters. The roughness signal is calculated in the direction normal to the fitted sphere. The spatial distribution of the asperities and their height were also extracted. In this regard, the asperities' centers of mass were first detected and then the peak-to-peak distances were calculated using a Voronoi tessellation. The height is calculated with respect to the minimum z-value in the scan [1]. The average asperity height *H*, the average inter-asperity distance *d* and the particle radius *R* are then used to calculate the dimensionless roughness parameter δ used in the main text.

To calculate the excess of area EA, the AFM data were analyzed in three steps. First, each particle center of mass was identified by finding the local maxima of a band-pass filtered image. Second, the radius of each particle was extracted by fitting its profile with a sphere. A squared region of interest was selected around each center such that the fitted radius had the least error. In this way, the region of interest only contains a spherical cross-section and excludes contributions from the neighbors. Finally, for the selected region of interest, the surface area for the scanned particle was calculated and normalized by the area of the ideal spherical cap reconstructed from the fitted radius. This value corresponds to the excess of area (EA). We then also extracted values of excess area in a standard fashion from BET measurements (EA_{BET})

The RMS roughness conventionally is defined as the root-mean-square of the surface vertical oscillations in the direction normal to the substrate and can be calculated as $RMS = \sqrt{\sum_{i=1}^{n} z_i^2}$, where z_i denotes the distance measured in the normal direction from the mean surface to the i-th data point; n is the total number of data points.

In Figure S4, we compare the four distinct roughness operators. The root-mean square roughness (RMS) follows the same trend of surface area-connected operators resulting insensitive to the particle size. All those operators are average quantities and do not specifically consider the dynamics of the three-phase contact line on rough surfaces. To link the surface roughness directly to contact line dynamics we have introduced a dimensionless roughness parameter $\delta = \frac{H}{d^2}R$, where H is the average asperity height, d the mean asperity-to-asperity distance and R the particle radius. In this way, provided that all the asperities have comparable shapes, it is possible to differentiate the wetting behavior of colloids having different sizes of the core but decorated with the same roughness amplitude. The use of δ highlights the importance of the number and size of the asperities providing possible pinning points. This is directly connected to the force required for contact angle depinning [2]. By examining the data reported in Figure S4, we notice that the parameter δ leads to a different roughness ranking, fully fitting the observations reported in the main text.

SI 3: Effect of the composition on the morphology and on the wetting of organic colloids

Thanks to the synthesis strategy presented in Section 1, it is possible to obtain organic particles with different surface roughness as shown in Figure 2 of the manuscript and **Figure S5**. At the same time though, imposing a shallower compositional gradient between the two monomers feeds (as for PS-III and PS-IV) leads to a more heterogenous polymers distribution on the particles surface. Thus, although a finer control of the surface topography is achieved, surface roughness and surface composition cannot be decoupled and tuned independently. Consequently, the particles wetting behavior reflects the heterogeneous nature of the particles' surface. The overall nature of the outer layer reflects the composition of the second feed and the timescales associated to its growth. In fact, at the two extremes,

sulfonated polystyrene at water-n-decane interfaces is hydrophobic[3, 4, 5] while polyacrylonitrile is hydrophilic (57°) and often used to hydrophilize polymer blends[6, 7]. The contact angles of the PS-III and PS-IV particles together with the hydrophobic reference smooth homo-polymer beads PS-I are reported in **Figure S5**.

The measured hydrophilicity of PS-III and PS-IV is indeed intrinsically due to their chemical composition and not an effect related to surface roughness, which is indeed very limited in both cases. PS-III and PS-IV only produce o/w irrespective from the input energy applied.

SI 4: Depinning energy

The energy associated to the dewetting of a single spherical asperity has been predicted to scale with the square of the asperity's height[1]. In particular

$E = \gamma \pi h^2 cos(\theta_0)$

where γ is the interfacial tension of the interface, h the asperity height and θ_0 is the contact angle of the smooth macroscopic material.

Knowing the average inter-asperity distance and the particle size, we can estimate the maximum number of pinning points that the contact line has to overcome to hop from the pinned state to its equilibrium state, i.e. the average number of asperities located at the particles' equator. This quantity can be used to estimate the energy that would take contact line to move beyond the equator, i.e. a characteristic energy to switch wettability (see Table S5). SiO_2-II emulsified from the apolar phase is directly transported through the interface already at low shear rates. Remarkably, PS-II has an estimated depinning energy from the equator smaller than SiO_2-II. Nevertheless, it can stabilize oil droplets despite its hydrophobic nature when dispersed initially in water and emulsified at low shear rates. An explanation for this fact may be that the pinning efficiency provided by the roughness, in this case, is enhanced by the presence of surface chemical heterogeneities [8]. The latter have been observed [9] and inferred for various PS colloids [10, 11]. Given the values reported in Table S5, for our experimental conditions, mechanical phase inversion via metastable wetting seems to be possible for depinning energies from the equator greater than ~10^4 k_BT for organic colloids and ~10^5 k_BT for inorganic particles. Interestingly, the window of allowed parameters for the mechanical phase inversion to take place is narrow. Thus, for too high energies, e.g. for SiO_2-IV_O at the water/n-decane interface, phase inversion is no longer achievable. The estimates presented in Table S5 are susceptible to considerable deviations since they rely on delicate quantities for which it is very difficult to have robust statistical values.

SI 5: Simulated equilibrium configuration at fluid-fluid interfaces

Here we describe the details of the numerical simulations. The surface of a raspberry-shaped colloid is represented in our model by a grid of points while the fluid-fluid interface at which the colloid is adsorbed is represented by another grid of points. The grid representing the raspberry-shaped colloid is obtained

by first defining a triangular grid with spherical shape, and then opportunely deforming it where the asperities are located. Given as input the position of the colloid and the surface tensions of the system (γ, γ_1, γ_2, i.e., respectively, the surface tension between the two fluids, between the colloid and fluid 1, and between the colloid and fluid 2, where fluid 1 is the fluid above the interface and fluid 2 is the fluid below), we numerically compute the equilibrium shape of the fluid-fluid interface by using a simulated-annealing approach [12, 13] to find the position of the fluid-fluid interface grid points that minimizes the thermodynamic potential

$$\Omega = \gamma S + \gamma_1 W_1 + \gamma_2 W_2 + P_1 V_1 + P_2 V_2, \quad (1)$$

with S the total area of the fluid-fluid interface, W_1 the surface area of the colloid wetted by fluid 1, W_2 the surface area of the colloid wetted by fluid 2, $P_1 V_1$ and $P_2 V_2$ the pressure-times-volume term for fluid 1 and fluid 2, respectively. Since in our model we assume an approximately flat fluid-fluid interface far away from the colloid, the term $P_1 V_1 + P_2 V_2$ is constant (so, can be neglected). For convenience, Ω is shifted by a constant and rewritten as

$$E = \gamma (S - A + W_1 \cos\theta) \quad (2)$$

where $\cos\theta \equiv (\gamma_1 - \gamma_2)/\gamma$ is the cosine of Young's contact angle θ, and A is the surface area of the fluid-fluid interface when there is no particle (so, A is a constant). Using this definition (Eq. (2)), E = 0 when the colloid is desorbed from the interface and completely immersed in fluid 2, and $E = \Sigma \gamma \cos\theta$ when the colloid is desorbed from the interface and completely immersed in fluid 1 (with Σ the total colloid surface area).

During the simulated annealing to compute the equilibrium shape of the fluid-fluid interface by minimizing E, the two fluids are allowed to exchange volume between one another. Therefore, the level of the interface far away from the colloid will automatically reach its equilibrium value at the end of the simulation (that is, during the simulation, the height of the colloid center of mass at the interface is automatically minimized with respect to E). In each simulation, the initial shape of the fluid-fluid interface is a flat plane at height $(-R \cos\theta)$ from the particle center of mass, with R the radius of the colloid, that is close to the expected equilibrium position. We consider only one particle orientation, assuming that any other orientation is qualitatively analogous.

The equilibrium shape of the fluid-fluid interface for the simulated raspberry-shaped colloid (R = 200 nm, γ = 0.053 N/m, $\theta = 70°$) is associated to an energy of adsorption $E = -0.62 \cdot 10^6 k_B T$, with k_B the Boltzmann constant and T room temperature. As a comparison, we compute analytically the energy E [Eq. (2)] of a smooth spherical colloid of radius R. Assuming gravity negligible, the sphere adsorbs at the fluid-fluid interface forming a contact angle θ and leaving the interface flat. So, using in Eq. (2) that $S-A = -\pi R^2 \sin\theta^2$ and $W_1 = 2\pi R^2 (1 - \cos\theta)$, we obtain

$$E_{sphere} = -\gamma \pi R^2 (1 - \cos\theta)^2. \quad (3)$$

For R = 200 nm, γ = 0.053 N/m, $\theta = 70°$, it follows $E_{sphere} = -0.70 \cdot 10^6 k_B T$, that is the smooth spherical colloid is more strongly bonded to the fluid-fluid interface than its raspberry counterpart. The reason is that the raspberry colloid induces capillary deformations, which have an energy cost.

SI 6: Quasi-static adsorption at fluid-fluid interfaces

In this section, we give the details of the calculations to reproduce the quasi-equilibrium adsorption of a raspberry-shaped colloid at the fluid-fluid interface, assuming that the initial position of the colloid is in fluid 1 (fluid above mimicking apolar phase), i.e. the fluid with lowest affinity with the particle surface, since we set $\theta = 70°$. The strategy we adopt is explained as it follows. As initial shape (say, the shape s0) of the fluid-fluid interface, we consider a flat plane at height h = 0.8 R (where h = 0 corresponds to the height of the particle center of mass), i.e. far from the interface equilibrium height expected around (−R cos θ) = 0.34 R. Using our numerical method (i.e. a simulated annealing simulation [12]), we compute the equilibrium shape of the fluid-fluid interface (i.e. with minimum E) with the constraint that each point of the interface grid cannot go at a distance greater than Δ = 0.05 R from its initial position (in that simulated annealing simulation). Once obtained the minimum-E shape of the fluid-fluid interface satisfying this constraint (say, the shape s1), we compute E for s1. We then perform another simulated-annealing simulation using s1 as initial shape of the fluid-fluid interface and using again the constraint that the interface grid points cannot explore at a distance greater than Δ from their initial position (now defined by s1). This process is repeated for 500 steps, with each simulated-annealing simulation using as initial interface shape the final shape of the previous simulated-annealing simulation. The sequence of interface shapes that we obtain represents (approximately) the quasi-equilibrium sequence of the shapes of the fluid-fluid interface when the colloid adsorbs from its initial position towards the equilibrium. The fix maximum displacement Δ in computing each minimum-energy shape imposes the evolution of the interface shape to approximately follow the steepest energy gradient path in the E($\mathbf{x}^N$) landscape, where $\mathbf{x}^N=\mathbf{x}_1,\mathbf{x}_2,...\mathbf{x}_N$ are the position in the 3D space of the N interface grid points (the smaller the Δ, the better the approximation). When the particle quasi-statically adsorbs at the interface, any energy barrier present in the energy landscape E is possibly able to trap the particle in a metastable configuration different than the equilibrium position.

To better interpret the results shown in Figure 8 in the main manuscript, in Figure S12 we show the energy E for three quasi-static simulations analogous to the three quasi-static simulations shown in Figure 8, but with the colloid directly located at its equilibrium position. Each of the three quasi-static simulations shown in Figure S12 consists of a sequence of 5 simulated-annealing simulations, where each simulated-annealing simulation consists of ~10^7 Monte Carlo steps. The data plotted in Figure S12 are the current energy E associated to the actual interface shape (conversely to Figure 8D, where only the final energy of each simulated-annealing simulation is reported. This enables to followed in "live-mode" (every 5000 Monte Carlo steps) the permitted fluctuations in the energy E that possibly allow the interface shape to overcome energetic barriers and eventually reach a lower minimum energy state. The initial temperature T_0 of each simulated-annealing simulation is $T_0 \cong 10^4 °C, 10^6 °C, 10^7 °C$ (the same as Figure 8D and the temperature is then decreased approximately linearly till zero thorough the simulated

annealing). As expected, the higher T_0, the greater are the fluctuations in E observed during each simulated-annealing simulation. For the quasi-static simulation with $T_0 \cong 10^{7}$°C, that in Figure 8D of the main manuscript corresponds to the colloid reaching the equilibrium (blue line), the fluctuations in E are ~$0.5 \cdot 10^6$ k_B T. For the quasi-static simulation with $T_0 \cong 10^{6}$°C, that in Figure 8D of the main manuscript corresponds to the colloid trapped in a metastable state close to the equilibrium (green line), the fluctuations in E are ~$0.3 \cdot 10^6$ k_B T. Finally, for the quasi-static simulation with $T_0 \cong 10^{4}$°C, that in Figure 8D corresponds to the colloid trapped in a metastable state far from the equilibrium (cyan line), the fluctuations in E are ~10^4 k_B T. Therefore, we can deduce that, in Figure 8D, the energy barriers that prevent the colloid, quasi-statically adsorbing at the interface, from reaching the equilibrium must be greater than ~10^4 k_B T and lower than ~$0.5 \cdot 10^6$ k_B T. This estimated regime of validity is compatible with the values proposed in Table S5. An approximate estimate of the energy barriers can be obtained by computing the difference in adsorption energies for smooth spheres (see Eq. 3) at equilibrium and at an effective contact angle corresponding to the metastable contact angle of the rough colloid. By taking the input metastable angle to be 99° (corresponding to position (d) in Figure 8 of the main text) and computing the energy difference relative to the equilibrium case of θ=70°, we get a value of $\Delta E \approx 0.4 \cdot 10^6$ k_B T, in line with the data showed in Figure 8 D. This approximation does not consider the energetic effect of the deformation of the interface.

SI 7: Colloidal synthesis

Inorganic Particles. The synthesis of inorganic raspberry-like particles has been carried out as follows. Silica nanospheres (berries) were anchored electrostatically onto larger, positively modified silica colloids (cores) [14, 15, 16]. In a typical procedure [17], either homemade Stöber silica particles [18, 19] (0.18wt%, R = 161 nm± 15 nm) or commercially available cores (1.5 wt%, R = 200 nm ± 20 nm, R = 295 nm ± 20 nm, Nanocym) were modified for 30 min in a 0.03 wt% aqueous solution of poly-DADMAC (50 ml) to render their surfaces positively charged. The suspension was then washed three times with milliQ water to remove the unbound excess of polyelectrolyte. Afterwards, the nanoparticle suspension containing the berries was added to the positively modified core colloids (0.45 wt% suspension). 39 nm (6.5 mL, 1 wt%) or 22 nm (88 µL, 48 wt%) silica nanoparticles (berries) were successfully adsorbed onto the surface of the cores during 30 min of vigorous stirring.

In order to tune the surface roughness, a sol-gel route[20] was used to smoothen the raspberry-like particles. A 5 vol% TEOS solution in EtOH was added to a mixture of EtOH/NH4OH/H2O (77:13:10 volumetric ratio) containing 0.011 wt% of raspberry-like particles at an injection rate of 2 mL per hour while sonicating. The injection of the silica precursor was split into periods of 8 min each, followed by 25 min of equilibration time. The smoothed raspberry-like particles were washed three times with milliQ water.

The smoothing step has the primary effect of tuning the particles' surface roughness and it furthermore strengthens the link between the core and the asperities preventing any possible detachment of the small colloids from the cores, even at high-shear emulsification. The parameters of the syntheses are found in the Table S4.

Covalent Surface Modification by Bromo-Silanes. As-produced raspberry-like particles can be surface-activated in a mixture of H2O2/NH4OH/H2O (volume ratio of 1:1:1, 3.3 wt/vol%) at 70 °C for 10 min. In this way, a uniform layer of silanol groups was created on the particles' surface enhancing the homogeneity and efficiency of the subsequent silanization step. This step is necessary when the IEP of the particles does not coincide with the IEP of native silica. The activated particles were washed by centrifugation/re-dispersion in deionized water and dried under reduced pressure at 60 °C. Afterwards, the particles were stirred overnight in a 2 wt% APTES solution in water. The APTES-modified particles were then washed by repeated centrifugation/re-dispersion cycles in ethanol and dried in a vacuum oven at 60 °C. The amino-functionalisation can be verified by means of a titration curve as reported in Figure S6. The final functionalization was achieved by grafting α-bromoisobutyryl bromide (0.2 ml, 1.6 mM) onto the amino-modified particles (0.9 wt%) by incubation in dry dichloromethane (5 mL) in the presence of triethylamine (0.4 mL). The reaction was carried out under inert atmosphere at room temperature. The suspension was then washed several times in dichloromethane and dried at 60 °C in a vacuum oven. Partially hydrophobized particles bearing bromo-silane groups were re-dispersed in polar and apolar solvents by sonication. The former is simplified by adding MeOH (50 vol%) which is eventually removed upon evaporation at reduced pressure.

Organic Particles. All organic particles are fabricated via a two-step semibatch emulsion polymerization [21, 22, 23]. In the first step, core particles were nucleated and grown in starved conditions, while feeding the first monomer mixture; afterwards, a further shell was grown onto them by switching to a second feed. The overall synthesis was adjusted according to the desired surface morphology [24], taking advantage from both the sequence of addition and feed compositions. In all cases, SDS was initially used as emulsifier for nucleation and the reactor was evacuated and flushed with nitrogen three times to avoid radical deactivation by oxygen. When working with AN, the addition of KPE as second surfactant after the particle nucleation stage improves the colloidal stability.

Smooth Particles. This section is referred to the synthesis of PS-I, which have been named as smooth particles (S). In the case of PS-I (the procedure presented hereafter refers to an initial 250 g batch, which will have eventually approximately 10% solid content), a mixture of water and surfactant (SDS) was charged into a glass reactor and the temperature set to 70 °C (ICS in Supporting Table S1). After the injection of 0.75 g of KPS dissolved in 20 g of water, an emulsion of styrene, DVB, water, and surfactant (CF1S) was fed at a rate of 0.074 mL/min for 1020 minutes by means of a HPLC pump. The slow addition ensures starved polymerization conditions. Meanwhile, a total solution of 95.6 g of water and 1.6 g of KPS was also continuously fed at 0.094 mL/min, to keep the radical concentration constant. The shell monomer solution (CF2S) was fed in the same reactor at a rate of 0.08 mL/min for 180 minutes right after terminating the first step. At the same time, the previous initiator feed was disconnected and 20 g

of water containing 0.2 g of KPS were added to keep the reaction running. After the addition of CF2S was completed, the latex was left running in batch until full conversion was obtained. The evolution of the polymer conversion and particle size was monitored hourly and a full final size characterization was performed via SEM (Supporting Table S3). This synthesis allows controlling the cross-linking density of the surface but not its surface morphology.

Rough Particles. This section is referred to the syntheses of PS-II, PS-III and PS-IV, which have been named as rough particles (R). In the syntheses, an initial charge (ICR) composed of water, monomer (100% AN), surfactant (SDS) and initiator (KPS) was injected in the reactor in the mass ratio shown in Supporting Table2 (the reported procedure presented hereafter refers to a 120 g of total mass, with 10% polymer solid content) and the mixture was heated up to 60 °C. Afterwards, 0.24 g of KPE dissolved in 4 ml of water were added to ensure colloidal stability. The evolution of polymer conversion and particle size was monitored on an hourly base by thermogravimetric analysis (T = 120 °C) using a HG53 Halogen Moisture Analyzer (Mettler Toledo, Switzerland) and by Dynamic Light Scattering (DLS, Malvern Zetasizer Nano Z, United Kingdom). The core particles were used directly as seeds for the shell growth once the conversion reached 90% (roughly after three hours) and without stopping the previous reaction. At that point, 0.18 g of KPS, dissolved in 4 g water, were injected and the second feed of monomer mixture was dispensed for four hours at a flow rate of 0.06 mL/min. Depending on the desired final morphology of the particle, different feed strategies were adopted to switch from the initial ICR to the composition of the final outer shell (St and DVB). In the case of the particles with maximum surface roughness (PS-II in the main manuscript), a feed of water, styrene and DVB (Charged Feed 1, CF1R in Supporting Table S2) was directly injected. For particles with a smoother surface, a more gradual change in the feed composition was imposed with the help of two pumps as schematically shown in Figure 2. In particular, the second mixture (Charge Feed 2, CF2R) was dripped into the vessel of the first feed in order to change its composition from CF1R to CF2R still keeping constant the total mass fraction of monomers in the feed added to the reactor, as shown in Supporting Figure S1. According to the desired morphology, 60 or 210 minutes were imposed for particle PS-III and PS-IV, respectively. After the gradient feed, CF2R was directly connected to the system for the remaining reaction time (i.e., 30 or 180 minutes). In all cases, after two hours the reaction mixture was further diluted with 20 g water to prevent aggregation. Similarly, to the case of the core, the evolution of particle size and monomer conversion was monitored during the whole shell synthesis. After the end of the second feed, the reaction vessel was left for half an hour at 60 °C to ensure full conversion (above 90%). After cooling, the produced polymer dispersion was filtered by a filter paper (MN 615, 22 s filtration speed) to remove possible polymer lumps. A full, final characterization of the particles size was assessed using SEM image analysis (Supporting Table S3).

SI 8: References

1. Zanini M, Marschelke C, Anachkov SE, Marini E, Synytska A, Isa L. Universal emulsion stabilization from the arrested adsorption of rough particles at liquid-liquid interfaces. *Nat Commun* **8**, 15701 (2017).

2. Ye M*, et al.* Superamphiphobic Particles: How Small Can We Go? *Phys Rev Lett* **112**, 016101 (2014).

3. Isa L, Lucas F, Wepf R, Reimhult E. Measuring single-nanoparticle wetting properties by freeze-fracture shadow-casting cryo-scanning electron microscopy. *Nat Commun* **2**, 438 (2011).

4. Maestro A, Guzmán E, Ortega F, Rubio RG. Contact angle of micro- and nanoparticles at fluid interfaces. *Curr Opin Colloid In* **19**, 355-367 (2014).

5. Paunov VN. Novel Method for Determining the Three-Phase Contact Angle of Colloid Particles Adsorbed at Air−Water and Oil−Water Interfaces. *Langmuir* **19**, 7970-7976 (2003).

6. Lim JW, Lee J-M, Yun S-M, Park B-J, Lee Y-S. Hydrophilic modification of polyacrylonitrile membranes by oxyfluorination. *J Ind Eng Chem* **15**, 876-882 (2009).

7. Abdallah H, Jamil Tarek S, Shaban AM, Mansor Eman S, Souaya Eglal R. Influence of the polyacrylonitrile proportion on the fabricated UF blend membranes' performance for humic acid removal. In: *Journal of Polymer Engineering* (ed^(eds) (2018).

8. Zanini M*, et al.* Detachment of Rough Colloids from Liquid–Liquid Interfaces. *Langmuir* **34**, 4861-4873 (2018).

9. Chen W, Tan S, Huang Z, Ng T-K, Ford WT, Tong P. Measured long-ranged attractive interaction between charged polystyrene latex spheres at a water-air interface. *Phys Rev E* **74**, 021406 (2006).

10. Kaz DM, McGorty R, Mani M, Brenner MP, Manoharan VN. Physical ageing of the contact line on colloidal particles at liquid interfaces. *Nat Mater* **11**, 138-142 (2012).

11. Wang A, McGorty R, Kaz DM, Manoharan VN. Contact-line pinning controls how quickly colloidal particles equilibrate with liquid interfaces. *Soft Matter* **12**, 8958-8967 (2016).

12. Soligno G, Dijkstra M, Roij Rv. The equilibrium shape of fluid-fluid interfaces: Derivation and a new numerical method for Young's and Young-Laplace equations. *J Chem Phys* **141**, 244702 (2014).

13. Soligno G, Dijkstra M, van Roij R. Self-assembly of cubic colloidal particles at fluid–fluid interfaces by hexapolar capillary interactions. *Soft Matter* **14**, 42-60 (2018).

14. Kamp M*, et al.* Selective Depletion Interactions in Mixtures of Rough and Smooth Silica Spheres. *Langmuir* **32**, 1233-1240 (2016).

15. Furusawa K, Anzai C. Preparation of composite fine particles by heterocoagulation. *Colloid Polym Sci* **265**, 882-888 (1987).

16. Harley S, Thompson DW, Vincent B. The adsorption of small particles onto larger particles of opposite charge Direct electron microscope studies. *Colloid Surface* **62**, 163-176 (1992).

17. Zanini M, Hsu C-P, Magrini T, Marini E, Isa L. Fabrication of rough colloids by heteroaggregation. *Colloid Surface A* **532**, 116-124 (2017).

18. Stöber W, Fink A, Bohn E. Controlled growth of monodisperse silica spheres in the micron size range. *J Colloid Interface Sci* **26**, 62-69 (1968).

19. Bogush GH, Tracy MA, Zukoski CF. Preparation of monodisperse silica particles: Control of size and mass fraction. *J Non-Cryst Solids* **104**, 95-106 (1988).

20. Graf C, Vossen DLJ, Imhof A, van Blaaderen A. A General Method To Coat Colloidal Particles with Silica. *Langmuir* **19**, 6693-6700 (2003).

21. Cingolani A, Cuccato D, Storti G, Morbidelli M. Control of Pore Structure in Polymeric Monoliths Prepared from Colloidal Dispersions. *Macromol Mater Eng* **303**, 1700417 (2018).

22. Landier C, Barandiaran MJ, Drujon X, Asua JM. Synthesis of Core/Shell Latexes in a Continuous Stirred Tank Reactor. *Ind Eng Chem Res* **43**, 700-707 (2004).

23. Evans CE, Lovell PA. Click chemistry as a route to surface functionalization of polymer particles dispersed in aqueous media. *Chem Commun*, 2305-2307 (2009).

24. Okubo M. Control of particle morphology in emulsion polymerization. *Makromol Chem-M Symp* **35-36**, 307-325 (1990).